



HAL
open science

Fully adaptive active polarimetric imager at $1.55\mu\text{m}$ for target detection (Orale)

Nicolas Vannier, Corentin Plassart, Matthieu Boffety, François Goudail, Patrick Feneyrou, Luc Leviandier, Frédéric Galland, Nicolas Bertaux

► To cite this version:

Nicolas Vannier, Corentin Plassart, Matthieu Boffety, François Goudail, Patrick Feneyrou, et al.. Fully adaptive active polarimetric imager at $1.55\mu\text{m}$ for target detection (Orale). 7th International Symposium on Optronics in Defence and Security (OPTRO 2016), Feb 2016, Paris, France. hal-01688718

HAL Id: hal-01688718

<https://hal.science/hal-01688718>

Submitted on 19 Jan 2018

HAL is a multi-disciplinary open access archive for the deposit and dissemination of scientific research documents, whether they are published or not. The documents may come from teaching and research institutions in France or abroad, or from public or private research centers.

L'archive ouverte pluridisciplinaire **HAL**, est destinée au dépôt et à la diffusion de documents scientifiques de niveau recherche, publiés ou non, émanant des établissements d'enseignement et de recherche français ou étrangers, des laboratoires publics ou privés.

Fully adaptive active polarimetric imager at 1.55 μm for target detection

Nicolas Vannier¹, Corentin Plassart¹, Matthieu Boffety¹, François Goudail¹, Patrick Feneyrou², Luc Leviandier², Nicolas Bertaux³, Frédéric Galland³

¹ *Laboratoire Charles Fabry, Institut d'Optique, RD 128, 91127 Palaiseau, France. Email: nicolas.vannier@institutoptique.fr*

² *Thales research and Technology - France, RD128, 91767 Palaiseau Cedex, France. Email: luc.leviandier@thalesgroup.com*

³ *Aix Marseille Université, CNRS, Centrale Marseille, Institut Fresnel, UMR 7249, 13013 Marseille, France. Email: nicolas.beraux@fresnel.fr*

KEY WORDS: polarimetric imaging, active imaging, image processing, decamouflage.

ABSTRACT

We present different polarimetric imaging modes implemented on our active adaptive infrared polarimetric imager for target detection. These modes have been tested on different realistic decamouflage scenarios to compare them and find the main characteristics of the scenes and the minimum complexity of the system to perform the detection.

1 INTRODUCTION

Active polarimetric imaging consists in illuminating the scene with light in a controlled polarization state, and in analyzing the polarization state of backscattered light. These systems can reveal contrasts not visible in classical intensity images and find many applications in such domains as machine vision, remote sensing, biomedical imaging, and industrial control [1, 2, 3]. For target detection applications, it has been recently shown that optimal contrast between a target of interest and the background can be obtained by acquiring a single image with the illumination and analysis polarization states adapted to the characteristics of the observed scene [4, 5, 6]. Such adaptive polarimetric imagers have been built and validated [5, 6, 7]. The system presented in Ref. [6] is based on infrared illumination at 1.55 μm and can acquire images at a few tens of meters. It can implement any illumination and analysis polarization state on the Poincaré sphere thanks to a polarization state generator (PSG) and an analyzer (PSA) both based on two liquid crystal variable retarders (LCVR). Its capabilities in the domain of decamouflage have been demonstrated [6].

This imager has the maximal number of polarimetric degrees of freedom, since it can address the whole Poincaré sphere both in illumination and analysis. It can thus implement the optimal imag-

ing strategy, but also any other polarimetric imaging mode that has less degrees of freedom. It is thus a precious tool for evaluating the performance of polarimetric imaging modes, and determining which has the best performance/complexity trade off for a given application. In this paper, we use this tool to compare the performance of different polarimetric imaging modes for detection of manufactured objects in natural environments. By extensive testing on realistic outdoor scenarios, we determine the main characteristics and degrees of freedom a polarimetric imaging system should have for this application.

The paper is organized as follows. In Section 2, we describe the principle of our adaptive polarimetric imager and in Section 3, the polarimetric imaging modes we perform are described. In Section 4, we compare this imaging modes on realistic decamouflage scenarios to find the minimum complexity the system should have for the detection. We draw some conclusions and perspectives in Section 5.

2 ACTIVE ADAPTIVE POLARIMETRIC IMAGING SYSTEM

The principle of an adaptive polarimetric imager is illustrated in Fig. 1.

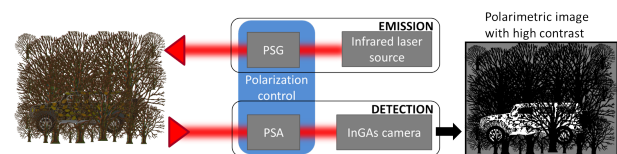


Figure 1: Principle of an adaptive scalar polarimetric imaging. PSG: Polarization State Generator. PSA: Polarization State Analyzer.

In this paper, we use the infrared imaging system presented in [6]. The system illuminates the scene with light coming from a laser source at 1.55 μm . Polarization state in illumination is defined by

a Stokes vector $I_{las}\mathbf{S}$ generated thanks to a Polarization State Generator (PSG), where I_{las} is the intensity of the laser and \mathbf{S} a unit norm, totally polarized Stokes vector. In the practical implementation we use, the PSG is composed of two Liquid Crystal Variable Retarders and one polarizer [7]. The polarimetric properties of a region of the scene corresponding to a pixel in the image is characterized by its Mueller matrix M . The Stokes vector of the light scattered by this region is $\mathbf{S}' = M\mathbf{S}$. It is analyzed by a Polarization State Analyser (PSA), which is a generalized polarizer whose eigenstate is the Stokes vector \mathbf{T} , where \mathbf{T} is a unit norm, totally polarized Stokes vector. As for the PSG, in the experimental setup we use, the PSA is composed of two Liquid Crystal Variable Retarders and one polarizer. An image is then formed on an intensity-sensitive InGAs camera which produces quarter VGA images (320x240). The measured signal at one pixel of coordinates (i, j) in the image has the expression of the Eq. 1.

$$I(i, j) = \frac{I_{las}}{2} \mathbf{T}^T M(i, j) \mathbf{S} \quad (1)$$

where the superscript T denotes matrix transposition and $M(i, j)$ is the Mueller matrix of the region of the scene corresponding to the pixel of coordinates (i, j) .

The PSG and the PSA can generate and analyze any polarization state on the Poincaré sphere. This polarization agility in illumination and analysis makes it possible to implement and compare different polarimetric imaging modes. The four modes that we consider in the present paper have been chosen to evaluate the influence of two key factors on the performance of polarimetric imaging: the number of polarimetric degrees of freedom and the normalization of the polarimetric image in the presence of complex backgrounds. These imaging modes are described in the following.

3 POLARIMETRIC IMAGING MODES

The performances of the four different modes are tested on a real-world scene (Fig. 2.a) consisting of a light grey painted metal plate partially overlaid with mud. The plate appears over a mud background and the scene, located 10m far from the imager, is representative of a surface laid mine detection scenario.

3.1 Fully adaptive scalar imaging

Fully adaptive scalar imaging [4, 6, 7] consists in acquiring a single polarimetric image while setting the

PSA and PSG so that the contrast between a target of interest and its surrounding background is maximal. If we assume that the target and the background are characterized by Mueller matrices M_t and M_b , the goal is to determine the PSG state \mathbf{S}_{opt} and PSA state \mathbf{T}_{opt} that optimize the contrast \mathcal{C} between these two regions. The proper expression of the contrast depends on the statistics of the perturbations that affect the image [8, 9]. For the sake of simplicity, we have chosen the expression in Eq. 2 of the contrast in this paper.

$$\mathcal{C}(\mathbf{S}, \mathbf{T}) = \frac{|\mathbf{T}^T D \mathbf{S}|}{\mathbf{T}^T (M_t + M_b) \mathbf{S}} = \frac{|\langle I_t \rangle - \langle I_b \rangle|}{\langle I_t \rangle + \langle I_b \rangle} \quad (2)$$

where $D = M_t - M_b$ is the difference of the Mueller matrices of the target and of the background regions and $\langle I_t \rangle$ and $\langle I_b \rangle$ the average intensities on the target and the background regions. The optimal PSG and PSA states are thus in Eq. 3.

$$(\mathbf{S}_{opt}, \mathbf{T}_{opt}) = \arg \max_{\mathbf{S}, \mathbf{T}} [\mathcal{C}(\mathbf{S}, \mathbf{T})] \quad (3)$$

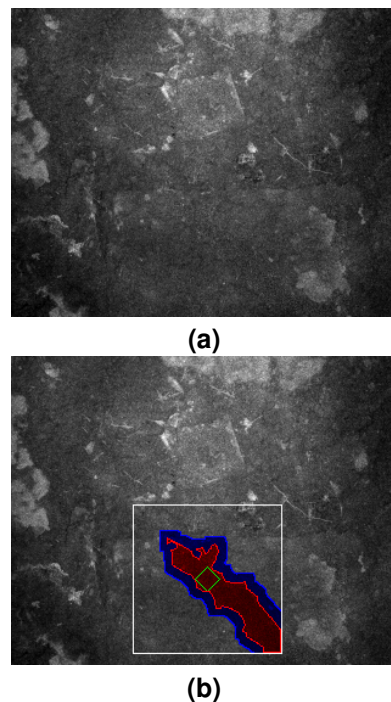


Figure 2: **(a)** Classical infrared intensity image of the scene. The contrast between the target and its background is $\mathcal{C} = 0.02$ (\mathcal{C} is defined in Eq. 2). **(b)** Image showing the designated initial location (green square), the corresponding ROI (white square), the segmented target region (red) and the local background region (blue).

Since in general both M_t and M_b are unknown, this optimization is not straightforward. To address this issue, a three-step adaptive strategy has been proposed in [7, 6]. First, the complete polarimetric

properties of the scene are measured by acquiring a Mueller image. Then a region of interest (ROI) is designated by an operator and is segmented in two regions using a fast active contour-based segmentation algorithm [10, 11] allowing us to determine the average Mueller matrices \hat{M}_t and \hat{M}_b inside the target and background regions respectively colored in red and blue in Fig. 2.b. Finally, the PSG and PSA states \mathbf{S}_{opt} and \mathbf{T}_{opt} that optimize the contrast between these two regions are determined, and an optimized polarimetric intensity image of the scene is acquired after implementing these states on the imager (Eq. 1). We have to note that this imaging mode requires full agility of PSG and PSA. The image obtained with this mode will be called the *fully adaptive scalar image*.

The Mueller matrices \hat{M}_t of the target (Fig. 2.b) and of its surrounding background \hat{M}_b are estimated after the segmentation step and reported in Tab. 1 as well as their difference \hat{D} . They allow us to determine the PSG and PSA states, \mathbf{S}_{opt} ($56^\circ, 16^\circ$) and \mathbf{T}_{opt} ($37^\circ, 3^\circ$) (the polarization states are represented by their azimuth and ellipticity (α, ϵ)), that optimize the contrast (see Eq. 2) between the target region and its surrounding background region.

The contrast is increased from $\mathcal{C} = 0.02$ in the intensity image to $\mathcal{C} = 0.27$ in Fig. 3. Fig. 3 shows the resulting optimized polarimetric image where the metal plate is now easily detected: the part of the plate that is not covered with mud appears in dark.

We note that other part of the scene appears in dark as the target but it is difficult to make the difference between the polarimetric response of the scene and its classical intensity reflection. In this case, the intensity variations throughout the scene hide the polarimetric contrast. A solution to this problem is to normalize polarimetric images as shown in the next section.

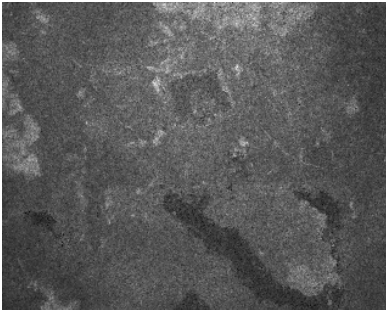


Figure 3: Fully adaptive scalar polarimetric image optimized for the target ($\mathcal{C} = 0.27$). The metallic plate appears in dark on the image.

\hat{M}_t	1.26×10^4	$\begin{pmatrix} 1.00 & 0.01 & 0.01 & -0.00 \\ -0.05 & 0.30 & 0.03 & 0.02 \\ -0.01 & 0.03 & -0.34 & -0.19 \\ -0.00 & -0.01 & 0.08 & -0.17 \end{pmatrix}$
\hat{M}_b	1.30×10^4	$\begin{pmatrix} 1.00 & 0.01 & 0.00 & 0.00 \\ -0.02 & 0.14 & 0.02 & 0.01 \\ -0.00 & 0.01 & -0.15 & -0.08 \\ -0.00 & -0.00 & 0.03 & -0.06 \end{pmatrix}$
\hat{D}	-0.42×10^4	$\begin{pmatrix} 1.00 & -0.06 & -0.06 & 0.16 \\ 0.90 & -4.66 & -0.51 & -0.27 \\ 0.12 & -0.54 & 5.43 & 3.06 \\ 0.09 & 0.40 & -1.35 & 3.36 \end{pmatrix}$

Table 1: Mueller matrices of the target of Fig. 3.b, of its surrounding background, and the difference \hat{D} of the two previous matrices.

3.2 Fully adaptive normalized scalar imaging

In real-world scenes, the backgrounds are often complex because they contain areas with very different intensity reflectivities even if their polarimetric properties are similar. The optimization of the contrast in scalar polarimetric imaging consist in adding a polarimetric contrast to the classical intensity contrast. In consequence, if the intensity reflectivity contrast is larger between the different regions in the background than between the target and the background region surrounding it, the intensity information is not useful and it is preferable to remove it. A simple way of doing so is to normalize the polarimetric images.

The principle of the *fully adaptive normalized scalar imaging* is exactly the same as the *fully adaptive scalar imaging*, with the only difference that the data used to calculate the optimal polarimetric states \mathbf{S}_{opt} and \mathbf{T}_{opt} are the normalized Mueller matrices \bar{M} defined for the Mueller matrices M as in Eq. 4.

$$\bar{M}_{kl} = \frac{M_{kl}}{M_{00}} \quad \forall [k, l] \in [0, 3] \times [0, 3] \quad (4)$$

The normalized Mueller image is now independent from multiplication with any spatially varying function. Indeed, if the Mueller image becomes $M(i, j) \times A(i, j)$, where $A(i, j)$ is a spatially varying scalar function, the normalized Mueller image $\bar{M}(i, j)$ is not modified. On the other hand, the information about intensity reflectivity that is present in the coefficient $M_{00}(i, j)$ is lost.

The optimal PSG and PSA states are found by optimizing the target/background contrast in the normalized Mueller image (Eq. 5).

$$\bar{\mathcal{C}}(\mathbf{S}, \mathbf{T}) = \frac{|\mathbf{T}^T \bar{D} \mathbf{S}|}{\mathbf{T}^T (\bar{M}_t + \bar{M}_b) \mathbf{S}} = \frac{|\langle I_t \rangle - \langle I_b \rangle|}{\langle I_t \rangle + \langle I_b \rangle} \quad (5)$$

where \bar{D} is equal to $\bar{M}_t - \bar{M}_b$.

The fully adaptive normalized scalar images are then obtained using Eq. 1 with arbitrary amplitude factor. This imaging mode still requires the estimation of the Mueller matrix of the scene by the imager.

Let us observe the scene in Fig. 2.a with this imaging mode. Fig. 4 represents the normalized scalar images obtained by optimizing the contrast on the target. The optimal states are now \mathbf{S}_{opt} ($56^\circ, 16^\circ$) and \mathbf{T}_{opt} ($37^\circ, 3^\circ$) with a polarimetric contrast of $\mathcal{C} = 0.25$. The local contrast has not changed, but since the fluctuations of intensity reflectivity have been removed, all the part of the target now clearly appear. In the presence of scenes with strong spatial fluctuations of intensity reflectivity and of illumination, thus appears very advantageous to normalize polarimetric images.

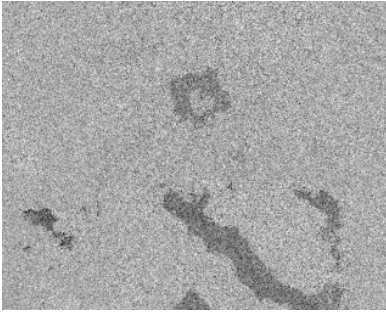


Figure 4: Fully adaptive normalized scalar polarimetric image optimized for the target ($\mathcal{C} = 0.25$).

3.3 Diagonal normalized scalar imaging

It can be seen in Tab. 1 that the target and background matrices, \hat{M}_t and \hat{M}_b , are mostly diagonal. Indeed, after measuring various Mueller matrices of real outdoor scenes, we have noticed that their diagonal coefficients are much higher than the others. It means that the observed objects are mostly depolarizing and that the polarimetric contrast is mainly due to a difference of depolarizing properties of the objects. As a consequence, the polarimetric imaging system can be simplified with reducing the number of polarimetric degrees of freedom while keeping good contrast enhancement performance.

Let us approximate the normalized Mueller matrix to its diagonal form (Eq. 6).

$$\bar{M} = \begin{pmatrix} 1 & 0 & 0 & 0 \\ 0 & \bar{M}_{11} & 0 & 0 \\ 0 & 0 & \bar{M}_{22} & 0 \\ 0 & 0 & 0 & \bar{M}_{33} \end{pmatrix} \quad (6)$$

by setting the non-diagonal coefficients to zero. The difference matrix \bar{D} is also diagonal and contrast op-

timization is very easy. Indeed, let us denote \mathbf{S}_H the Stokes vector representing linear horizontal polarization, \mathbf{S}_V the vertical one, \mathbf{S}_{45} and \mathbf{S}_{-45} those oriented at $\pm 45^\circ$, \mathbf{S}_L and \mathbf{S}_R the left circular and the right circular states. When the Mueller matrices of the target and the background are diagonal, the only combinations of polarimetric states we have founded by the optimization that can maximize the contrast defined in Eq. 5 are the following:

- $\{\mathbf{S}_{opt} = \mathbf{S}_H, \mathbf{T}_{opt} = \mathbf{S}_H\}$ or $\{\mathbf{S}_{opt} = \mathbf{S}_H, \mathbf{T}_{opt} = \mathbf{S}_V\}$.
- $\{\mathbf{S}_{opt} = \mathbf{S}_{45}, \mathbf{T}_{opt} = \mathbf{S}_{45}\}$ or $\{\mathbf{S}_{opt} = \mathbf{S}_{45}, \mathbf{T}_{opt} = \mathbf{S}_{-45}\}$.
- $\{\mathbf{S}_{opt} = \mathbf{S}_L, \mathbf{T}_{opt} = \mathbf{S}_L\}$ or $\{\mathbf{S}_{opt} = \mathbf{S}_L, \mathbf{T}_{opt} = \mathbf{S}_R\}$.

In the following, the image optimized under the hypothesis that Mueller matrices are diagonal will be called *diagonal normalized scalar image*. The advantage of this mode compared to fully adaptive normalized polarimetric imaging is that the optimization is simpler and it will be shown in the next section that under the hypothesis that the Mueller matrix is diagonal, the Mueller matrix of the scene can be obtained with only six images.

In the case of the scene in Fig. 2.a, the optimal states that optimize the contrast on the target are, $\mathbf{S}_{opt} = \mathbf{S}_{45}$ and $\mathbf{T}_{opt} = \mathbf{S}_{45}$. It is seen that the polarimetric contrast $\mathcal{C} = 0.19$ in the optimized diagonal normalized scalar image (Fig. 5) is quite close to those obtained with the fully adaptive normalized scalar imaging mode (see Fig. 4). It can be concluded that the impact of the reduction of the number of polarimetric degrees of freedom on contrast optimization performance is small. It will be seen in Section 4 that it is a general behavior of natural backgrounds.

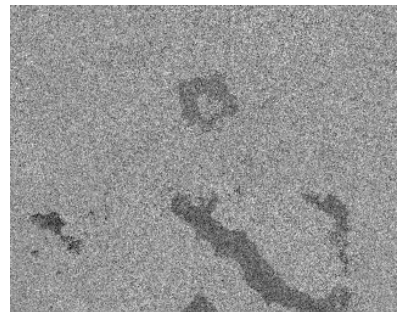


Figure 5: Diagonal normalized scalar polarimetric image optimized for the target ($\mathcal{C} = 0.31$).

3.4 Orthogonal States Contrast - OSC

We have seen that normalization is very important and that in natural backgrounds, Mueller matrices are mostly diagonal. Consequently, it is interesting to consider simpler imaging methods that involve acquisition of less than 16 images and are normalized. For that purpose, let us first consider acquiring the two intensity images (Eqs. 7 and 8).

$$I_1(i, j) = \mathbf{S}^T M(i, j) \mathbf{S} \quad (7)$$

$$I_2(i, j) = \mathbf{S}_\perp^T M(i, j) \mathbf{S} \quad (8)$$

where $M(i, j)$ is the Mueller matrix at the pixel with the coordinates (i, j) , \mathbf{S} is a unit norm, totally polarized Stokes vector and \mathbf{S}_\perp represents the opposite state in the Poincaré sphere of \mathbf{S} . From these two images a normalized image called *orthogonal state contrast* (OSC) [12, 13] is calculated (Eq. 9).

$$\rho(i, j) = \frac{I_1(i, j) - I_2(i, j)}{I_1(i, j) + I_2(i, j)} \quad (9)$$

We note that as in section 2.3.2, this image is independent from the multiplication of the Mueller image by any spatially-varying function. Moreover, since the intensity information is present in the images $I_1(i, j)$ and $I_2(i, j)$, knowledge of both $\rho(i, j)$ and $I_1(i, j) + I_2(i, j)$ gives access to both intensity and polarization information.

In practice, we will compute three *OSC* images from the acquisition of three image pairs: ρ_{HV} obtained with $\mathbf{S} = \mathbf{S}_H$, ρ_{45} obtained with $\mathbf{S} = \mathbf{S}_{45}$, and ρ_{LR} obtained with $\mathbf{S} = \mathbf{S}_L$. We have shown that if the Mueller matrix is strictly diagonal, these three OSC images are estimates of the normalized diagonal coefficients \bar{M}_{11} , \bar{M}_{22} and \bar{M}_{33} of the Mueller matrix at each pixel (i, j) .

Furthermore, it can be interesting, rather than displaying only one gray scale OSC image, to represent simultaneously the three OSC images as a single RGB-encoded color image, where the *red* channel is $\rho_{HV}(i, j)$, the *green* channel, $\rho_{45}(i, j)$, and the *blue* channel, $\rho_{LR}(i, j)$. We will call this color image the *3-OSC image*. It should be noted that since this image is obtained using 6 predefined combinations of illumination and analysis polarization states, it does not require prior acquisition of the Mueller matrix, image segmentation nor optimization of the illumination and analysis polarization states.

Fig. 6 displays the 3-OSC image of the scene in Fig. 2.a. The contrast on the target is $\mathcal{C} = [0.35, 0.35, 0.28]$ for the three channels. The contrast is close to that obtained with the fully adaptive normalized scalar imaging mode of Fig. 4 and all the parts of the target are easy to see thanks to the normalization. In consequence, similar results to

that obtained in the fully adaptive normalized scalar imaging can be obtained with less well selected images.



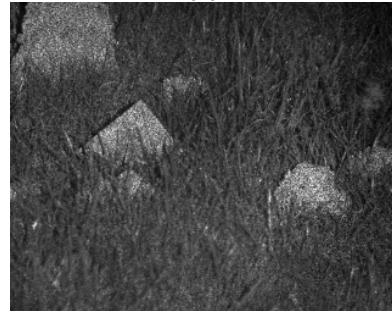
Figure 6: 3-OSC image of the same scene ($\mathcal{C} = [0.35, 0.35, 0.28]$).

4 APPLICATION ON OTHER SCENARIOS

In order to validate the results presented in section 3, we show two representative scenarios of man-made objects detection.



(a)



(b)

Figure 7: (a) Classical infrared intensity image of the scene ($\mathcal{C} = 0.26$). (b) Fully adaptive normalized scalar polarimetric image optimized for the target ($\mathcal{C} = 0.35$).

4.1 Object in vegetation

The scene in Fig. 7.a represents a light grey metal plate located 10m away from the imager and hid-

den in a mixed grass and dirt background. The target is easy to see on the grass but difficult to discriminate with dirt. Even if the contrast is improved between the target and its surrounding background in the fully adaptive normalized scalar polarimetric image (Fig. 7.b), it is still difficult to know where is the metal plate among the dirt parts because of the classical intensity information.

By normalizing with the intensity, the fully adaptive normalized scalar polarimetric image, the diagonal normalized scalar polarimetric image and the 3-OSC image reveal the target. The detection is then easy with the two last modes but the 3-OSC image do not need any optimization phase for an equivalent result.

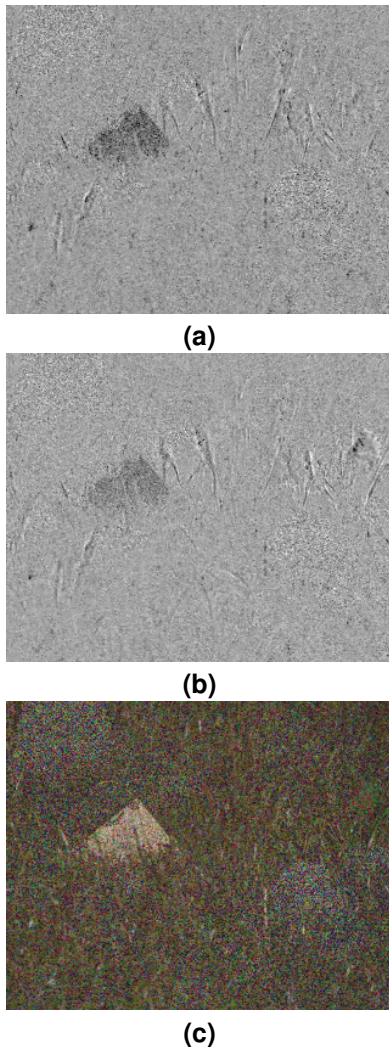


Figure 8: **(a)** Fully adaptive normalized scalar polarimetric image optimized for the target ($C = 0.21$). **(b)** Diagonal normalized scalar polarimetric image optimized for the target ($C = 0.13$). **(c)** 3-OSC image of the same scene ($C = [0.30, 0.31, 0.34]$).

4.2 Object on asphalt

The scene in Fig. 9.a represents a plastic object located 10m away from the imager and lying on an asphalt background. The illumination incidence is about 30° . Some parts of the asphalt surface are wet, and appear darker because water absorbs the $1.5\mu\text{m}$ emitted laser light that we are using. The presence of the wet regions makes it difficult to detect the object, which also appears dark. This scene may be representative of detection of hazardous objects on airport runways.

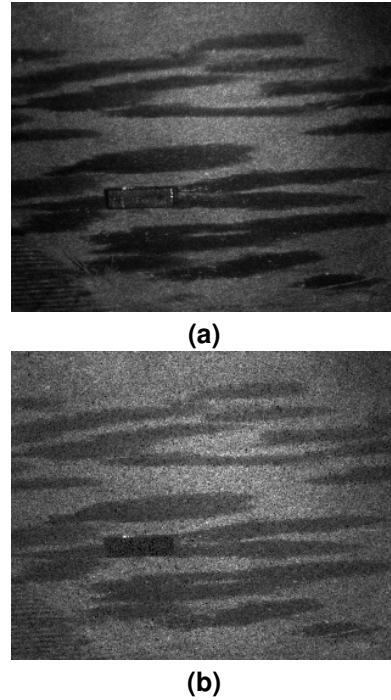


Figure 9: **(a)** Classical infrared intensity image of the scene ($C = 0.14$). **(b)** Fully adaptive scalar polarimetric image optimized for the target ($C = 0.20$).

Fig. 9.b represents the fully adaptive scalar image. It is observed that the contrast of the object is increased from $C = 0.14$ in the intensity image to $C = 0.20$ in the fully adaptive scalar image, but it remains nearly as dark as the wet parts of the background so that it is barely visible. On the other hand, in the fully adaptive normalized scalar image (Fig. 10.a) with a contrast of $C = 0.43$, in the diagonal normalized scalar polarimetric image optimized for the target (Fig. 10.b) with a contrast of $C = 0.31$ and in the 3-OSC image (Fig. 10.c) with a contrast of $C = [0.36, 0.35, 0.50]$, normalization removes the intensity reflectivity contrast between the different regions of the background and the object appears clearly thanks to its polarimetric contrast. This result illustrates again the usefulness of normalization

in the presence of backgrounds with high intensity reflectivity variations.

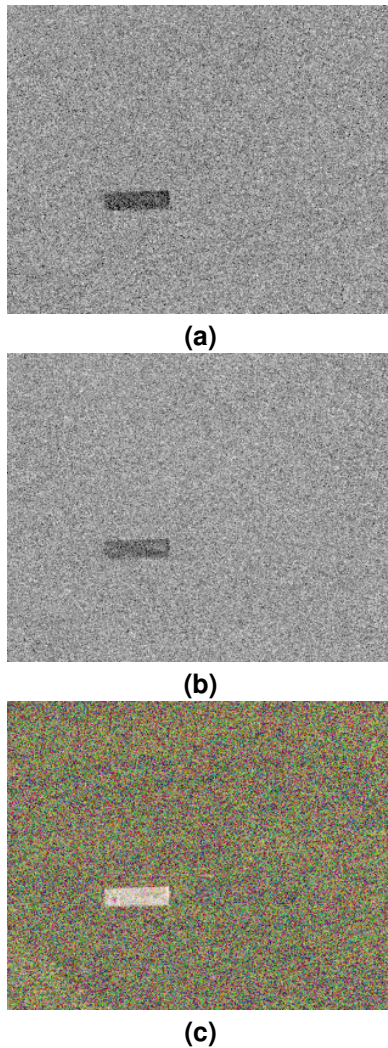


Figure 10: **(a)** Fully adaptive normalized scalar polarimetric image optimized for the target ($C = 0.43$). **(b)** Diagonal normalized scalar polarimetric image optimized for the target ($C = 0.31$). **(c)** 3-OSC image of the same scene ($C = [0.36, 0.35, 0.50]$).

5 CONCLUSION

We have addressed detection of manufactured objects in different types of backgrounds using active polarimetric imaging. We had at our disposal a fully adaptive imager that allowed us to compare different imaging modes having different number of polarimetric degrees of freedom, and thus different complexities. This study allowed us to underline the characteristics that a polarimetric imager designed for this type of applications should possess.

The first important result is that in most encountered scenarios, the Mueller matrices of the target

and of the background are mostly diagonal. In other words, the main source of contrast is the difference of depolarization. Consequently, the value of the contrast varies little with azimuth and ellipticities of PSG and PSA. Sufficient detection performance can thus be obtained with simpler polarimetric imaging systems having less degrees of freedom and thus being easier to build and to calibrate.

Another important result is that in many scenarios, the spatial variations of the intensity reflectivity in the scene are large. This may be due to spatial non uniformity of the illumination beam, or to the presence of complex backgrounds including regions that have very different intensity reflectivities. In this case, the intensity contrast between different regions of the background is dominant, and should thus be suppressed to better reveal polarimetric contrast. This can be done by normalizing the polarimetric images.

In conclusion, polarimetric target detection in natural environments can be efficiently performed by OSC imaging. Since the polarimetric properties of backgrounds vary much less spatially than their intensity reflectivity, the background of the OSC image is much smoother than that of the intensity image, which facilitates visualisation and identification of the objects. Moreover, it is to be noted that to calculate a normalized image, two intensity images have to be acquired, so that this mode gives access to both intensity and polarization information.

An attractive perspective to this work would be to study more in depth the physical information about the scene brought by each of the three channels of the OSC image. In particular, the circular component is more difficult to acquire with current technologies, based for example on Wollaston prisms [12] or micro-grid arrays [14], and it is important to determine in which case it is really necessary. It would also be interesting to study an efficient way of representing intensity and OSC information on the same image.

This work has been supported by the Agence Nationale de la Recherche (ANR) and the Direction Générale de l'Armement (DGA) under grant ANR-12-ASTR-0011-01 AUTOPOL. Nicolas Vannier's Ph.D thesis is supported by the DGA, Mission pour la Recherche et l'Innovation Scientifique (MRIS).

References

- [1] J. S. Tyo, M. P. Rowe, E. N. Pugh, and N. Engheta, "Target detection in optical scattering media by polarization-difference imaging," *Applied Optics* **35**, 1855–1870 (1996).

- [2] Y. Y. Schechner, S. G. Narasimhan, and S. K. Nayar, "Polarization-based vision through haze," *Appl. Opt.* **42**, 511–525 (2003).
- [3] A. Pierangelo, A. Benali, M.-R. Antonelli, T. Novikova, P. Validire, P. Gayet, and A. De Martino, "Ex-vivo characterization of human colon cancer by Mueller polarimetric imaging," *Optics Express* **19**, 1582–1593 (2011).
- [4] F. Goudail and A. B ni re, "Optimization of the contrast in polarimetric scalar images," *Opt. Lett.* **34**, 1471–1473 (2009).
- [5] G. Anna, H. Sauer, F. Goudail, and D. Dolfi, "Fully tunable active polarization imager for contrast enhancement and partial polarimetry," *Applied Optics* **51**, 5302–5309 (2012).
- [6] N. Vannier, F. Goudail, C. Plassart, M. Bofety, P. Feneyrou, L. Leviandier, F. Galland, and N. Bertaux, "Active polarimetric imager with near infrared laser illumination for adaptive contrast optimization," *Appl. Opt.* **54**, 7622–7631 (2015).
- [7] G. Anna, N. Bertaux, F. Galland, F. Goudail, and D. Dolfi, "Joint contrast optimization and object segmentation in active polarimetric images," *Optics Letters* **37**, 3321–3323 (2012).
- [8] P. R fr gier and F. Goudail, "Invariant polarimetric contrast parameters for coherent light," *J. Opt. Soc. Am. A* **19**, 1223–1233 (2002).
- [9] G. Anna, F. Goudail, and D. Dolfi, "Optimal configurations for active polarimetric imaging systems in the presence of different sources of poisson shot noise," *Optics Communications* **291**, 116 – 123 (2013).
- [10] F. Galland and P. R fr gier, "Minimal stochastic complexity snake-based technique adapted to an unknown noise model," *Optics Letters* **30**, 2239–2241 (2005).
- [11] N. Bertaux, F. Galland, and P. R fr gier, "Multi-initialisation segmentation with non-parametric minimum description length snake," *Electronics Letters* **47**, 594–595 (2011).
- [12] A. B ni re, F. Goudail, M. Alouini, and D. Dolfi, "Design and experimental validation of a snapshot polarization contrast imager," *Appl. Opt.* **48**, 5764–5773 (2009).
- [13] M. Alouini, F. Goudail, A. Grisard, J. Bourderionnet, D. Dolfi, A. B ni re, I. Baarstad, T. L ke, P. Kaspersen, X. Normandin, and G. Berginc, "Near infrared active polarimetric and multi-spectral laboratory demonstrator for target detection," *Appl. Opt.* **48**, 1610–1618 (2009).
- [14] D. A. LeMaster, "Stokes image reconstruction for two-color microgrid polarization imaging systems," *Opt. Express* **19**, 14604–14616 (2011).